



Eidgenössische Technische Hochschule Zürich
Swiss Federal Institute of Technology Zurich



Dynamic Causal Modelling during Intuitive Physical Inference and Perception of Falling Objects

Semester Project

Yihui Du
yihudu@student.ethz.ch

Neural Control of Movement Laboratory
Department of Health Sciences and Technology, D-HEST
ETH Zürich

Supervisors:
Gabrielle Zbären
Prof. Dr. Nicole Wenderoth

21.03.2022 – 30.06.2022

Contents

Contents	ii
1. Introduction	1
2. Materials and Methods	2
2.1. Subjects	2
2.2. Experimental task.....	2
2.3. Selection of regions of interest.....	3
2.4. General linear model.....	3
2.5. Dynamic causal modelling (DCM).....	3
2.5.1. Timeseries extraction of regions of interest	3
2.5.2. DCM specification	4
2.5.3. Parameter estimation and comparison	5
2.5.4. Comparison of connectivity strength between the physical inference and perception tasks	6
3. Results	7
3.1. Influence of physical inference on connectivity	7
3.2. Influence of perception on connectivity	8
3.3. Comparison of connectivity strength during physical inference and perception	8
4. Discussion	11
References.....	13
A. Appendix	14

1. Introduction

How do humans have a quick intuitive grasp of the world's physical structure and dynamics is an interesting question about physical inference. For instance, imagine a laptop unsteadily supported by a plastic swimming pool - we can easily know intuitively that the laptop would fall in the water or on the ground if the pool were pressed. Such physical scene understandings link perception with higher cognition, but the neural mechanisms underlying them in the brain remain unclear.

Intuitive physical inference specifically refers to the ability of people to use physical intuition to understand and predict the behavior of objects in the world. Studies on intuitive physical inference suggest that there might be a mental "intuitive physics engine" (IPE) in the brain, a cognitive mechanism like computer engines that simulate rich physics in video games (1). Several recent fMRI experiments identified a set of brain regions that are active during intuitive physical inference from visually presented scenes, comprising visual, parietal, and dorsal premotor regions (2). Interestingly, some of these regions overlap with brain regions involved in perception and visual imagery, such as visual and parietal areas (3). It has also been shown that early visual regions encode the content of visual imagery (4). However, previous studies of physical inference have not looked at how these regions interact with each other when making physical predictions.

Here, we study the effective connectivity between brain regions that have been shown to be involved in both physical inference and perception, and characterize the differences in neural interactions within this network between physical inference versus perception. For this, we modelled the network of overlapping brain regions during a physical inference task and a perception task involving falling objects, using dynamic causal modelling (DCM) (5,6,10). We selected three brain regions: superior parietal lobule (SPL), supramarginal gyrus (SMG) and early visual regions, and studied whether subjects have different driving input locations and/or different modulatory inputs between these regions during a physical inference task compared to a perception task. Specifically, we expected the DCM during physical inference to reflect driving inputs entering higher-order cognitive brain areas (i.e., SPL and/or SMG) and modulatory inputs to predominantly increase top-down connectivity, and the DCM during perception to reflect driving inputs entering visual cortex and modulatory inputs to predominantly increase bottom-up connectivity.

The aim of our analysis of connectivity parameter estimation was to test quantitative hypotheses about model parameters rather than perform a qualitative model structure selection. Thus, we performed group-level analyses of the estimated DCM parameters of single subjects, and assessed differences in mean connection strength between the physical inference and the perception tasks.

2. Materials and Methods

2.1. Subjects

Twenty healthy adult volunteers participated in the fMRI experiment and four had to be excluded from the analyses. The final sample included 16 participants (10 females, 6 males, age range 21-52 years old).

2.2. Experimental task

Each participant performed a physical inference task in the scanner, after having been trained to perform the task outside of the scanner. Participants had to alternately perform a control task, which was matched for visual inputs.

One trial of the physical inference task, which is referred to as simulation condition, works as follows (figure 1A, top row): An orange box with a ball attached to it enters the screen from either side and moves horizontally with a certain height and velocity. When the box reaches the middle of the screen, the ball drops and an occluder appears simultaneously. Participants' task is to press a button as soon as they think the ball lands on the ground. During one "catch trial" every six trials, participants additionally need to indicate the estimated landing location of the ball by moving a black rectangle. During the entire task, there is a fixation cross in the middle of the screen, which the participants were asked to fixate. This ensured that there were no unnecessary eye movements.

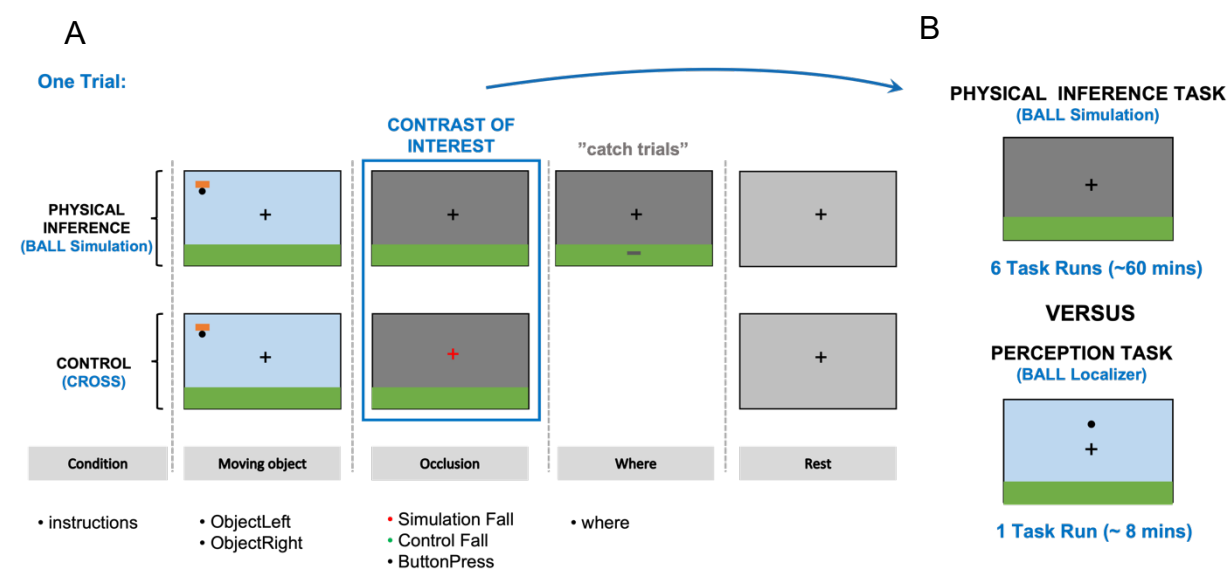


Figure 1: Intuitive physical inference fMRI experiment paradigm. (A) The top and bottom panel shows one sample sequence of a simulation and control trial, respectively. The occlusion-column represents the time frames used for the contrast of interest in the GLM analysis. (B) The top panel shows the occluded scene of the falling ball that the subjects needs to simulate. The bottom panel shows the scene of the falling ball that was seen by the subjects in the perception task.

The control trial of the physical inference task (figure 1A, bottom row) is similar to the simulation trial, except that participants have to press a button as soon as the color of the fixation cross changes instead of having to indicate the landing time of the ball. During this control trial, the participants received the same visual inputs and performed the same hand movements as in the simulation trial, but without imagining and predicting the time and location of the falling ball.

After having completed the physical inference task, participants additionally performed a perception task in the scanner. During this perception task (figure 1B, bottom panel), participants only had to passively watch a ball fall multiple times, without having to infer the trajectory of the ball behind an occluder or having to press a button. The trajectories of the falling ball were the same as the ones in the physical inference task.

2.3. Selection of regions of interest

The selection of ROIs for the DCM analysis was based on a previously performed conjunction analysis between the physical inference task and the perception task, which revealed overlapping activity in the right superior parietal lobule (SPL) and the right supramarginal gyrus (SMG). Additionally, we defined one ROI in right early visual cortex (covering V1, V2 and V3). Thus, the DCM contained three regions.

2.4. General linear model

All analyses were performed using the statistical parametric mapping (SPM12) software and customized MATLAB scripts.

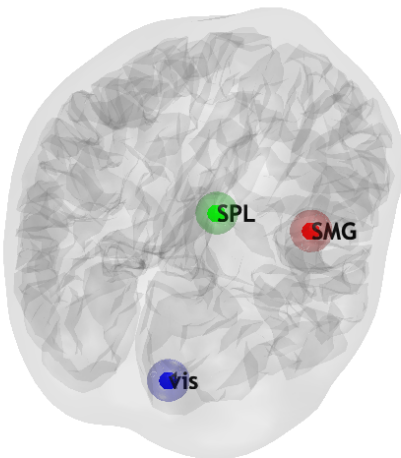
The general linear model (GLM) analysis was first specified and estimated on the single-subject level, with the data and regressors concatenated over six runs for the subsequent timeseries extraction. For the physical inference task, there were 7 task regressors modelling the instructions, moving object, occlusion in the simulation condition, occlusion in the control condition, where, button presses, and missed trials with no button presses (figure 1A). The nuisance regressors included white matter (WM) timeseries, cerebrospinal fluid (CSF) timeseries, and six movement parameters (three translation parameters and three rotation parameters), together with scrubbing regressors that scrub off any volume displaying motion bigger than half a voxel size. In the design matrix, we used hemodynamic response function (HRF) as the basis function for convolution and added the first temporal derivatives of the 7 task regressors. For the perception task, the design matrix contained the onsets and durations of the falling balls as a regressor of interest, combined with the same nuisance regressors as in the design matrix of the physical inference task described above.

2.5. Dynamic causal modelling (DCM)

2.5.1. Timeseries extraction of regions of interest

To extract the timeseries in our three regions of interest (ROIs), we defined a group 16mm sphere centred on peak coordinates derived from the previous conjunction analysis (see section

2.3). To allow for subject-specificity in the exact selection of voxels, we extracted timeseries from an 8 mm sphere centred on the subject-specific local maximum of the contrast image (simulation > control for the physical inference task, and falling ball > rest for the perception task) within the outer 16 mm sphere. This approach ensures that the subject-specific ROIs are close to the average group activity while accounting for slight variation in functional anatomy between participants. To select the voxels from which to extract the timeseries within each ROI, we used a t-contrast ($p < 0.001$ uncorrected) between the simulation and control conditions (simulation > control) for the physical inference task, and between the falling ball and the rest phases for the perception task (falling ball > rest).



Region name	Location (mm)
Early Visual Cortex (V1/V2)	9 -88 -14
Superior Parietal Lobule (SPL)	12 -66 56
Supramarginal Gyrus (SMG)	40 -42 42

Figure 2: The left figure shows the locations of three ROIs (8 mm spheres) from an example subject. The right table lists the coordinates of the three selected group peaks for DCM timeseries extraction.

For each subject, timeseries were extracted from every voxel of the contrast-masked ROIs. The signals were subsequently adjusted based on an F-contrast that retained the experimental effects of interest and regressed out task-unrelated variance specified by the nuisance regressors. The first principal component (eigenvariate) of each region's adjusted data was then used as the timeseries for subsequent DCM analyses.

2.5.2. DCM specification

To characterize the effects of physical inference and perception on effective connectivity between the ROIs, we applied dynamic causal modelling (DCM) (7). The classical deterministic DCM uses the following bilinear differential equation to infer effective connectivity parameters:

$$\dot{z} = \left(A + \sum_{j=1}^M u_j B^j \right) z + Cu$$

The variable z describes neuronal activity resulting from the dynamic interplay of three different influences (i.e., A, B and C). First, the A matrix represents endogenous or fixed connectivity during baseline, without external stimulation. Second, the elements in the B matrix represent the changes in connectivity modulated by experimental influences u . Finally, the matrix C denotes the direct influence of each experimental input u . We selected the condition 'simulation' as the experimental input u in the physical inference task, and 'falling ball' in the perception task. This neuronal model is coupled to a hemodynamic model of neurovascular coupling and the BOLD response, which together predict the BOLD timeseries (8). After DCM specification, the model is inverted to estimate the neural connectivity parameters by maximising negative free energy. We specified and inverted DCMs for the physical inference and perception tasks separately.

Importantly, each brain region in this model is equipped with an inhibitory self-connection (9). This is implemented by splitting the connectivity matrix A and modulatory input matrices B into two parts: extrinsic between-region connectivity and intrinsic within-region self-inhibition, with -0.5Hz as the default strength of the self-connections. Therefore, the more positive the self-connection parameter, the more self-inhibited the region, and so the less it will respond to inputs from the network. Conversely, the more negative the self-connection parameter, the less inhibited the region. For the extrinsic connectivity between regions, a positive value corresponds to an increase in connectivity, and a negative value to a decrease in connectivity.

2.5.3. Parameter estimation and comparison

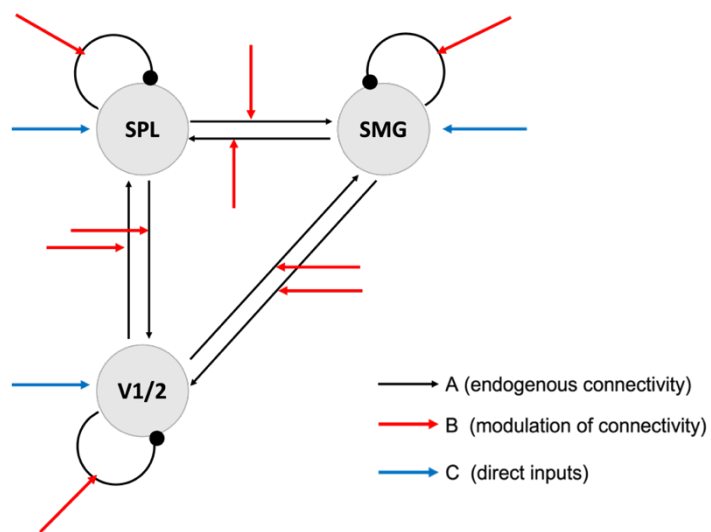


Figure 3: The network structure of our defined bilinear two-state full DCM. The model space is formed of the full model and all possible reduced models in which one or more connectivity and/or driving input parameters have been switched off.

We first defined a fully connected model of endogenous connectivity (represented by the A matrix) between the three selected ROIs because these regions are anatomically connected to each other (figure 3). To test hypotheses about changes in connectivity at the group level, we used the parametric empirical Bayesian (PEB) approach to estimate the connectivity parameters and their posterior probabilities on the group level (10). In short, the PEB scheme uses Bayesian model reduction (BMR) to invert a hierarchical Bayesian model of between subject effects on

within-subject parameters, with a GLM of between-subject effects (11). PEB can automatically search over all nested models; after the full model is estimated for each subject, the full PEB model is compared against nested PEB models and the parameters that don't contribute to the minimization of free energy are pruned. Finally, the average parameters over reduced DCMs weighted by their evidence are calculated to obtain a set of Bayesian model averages (BMAs), which represent the strength of each connection (i.e., A matrix) and the effects of experimental manipulations (i.e. B and C matrices). The parameter estimates (pe) of self-connections (A matrix) and self-modulations (B matrix) are unitless log scaling parameters that scale (i.e., multiply up or down) the default value of -0.5Hz, while the parameters of driving inputs (C matrix), between-region connections (A matrix) and between-region modulations (B matrix) are in units of Hz.

2.5.4. Comparison of connectivity strength between the physical inference and perception tasks

After computing the PEB estimation for the physical inference and perception tasks separately, the two models were compared using frequentist statistics to evaluate the difference of parameter estimates of the single-subject full models between the physical inference and perception tasks. For each parameter estimate ($N = 9$), a paired t-test was computed and a Bonferroni correction applied.

We first applied paired t-tests between the physical inference and perception tasks using each of the 16 subjects' estimated parameters of the full model. However, this approach ignores the uncertainty at the between-subject level and assumes that every subject contributes equally well to the group estimation of parameters. Thus, in a second statistical analysis, we additionally set a threshold of posterior probabilities at 0.7 and removed the single-subject estimates whose probabilities fell below this threshold from the group parameter comparison.

3. Results

3.1. Influence of physical inference on connectivity

To identify where the driving and modulatory inputs are exerted by physical inference, we constructed a full group-level (PEB) model on the A, B and C matrices, and used BMR to prune any effects not contributing to the model evidence.

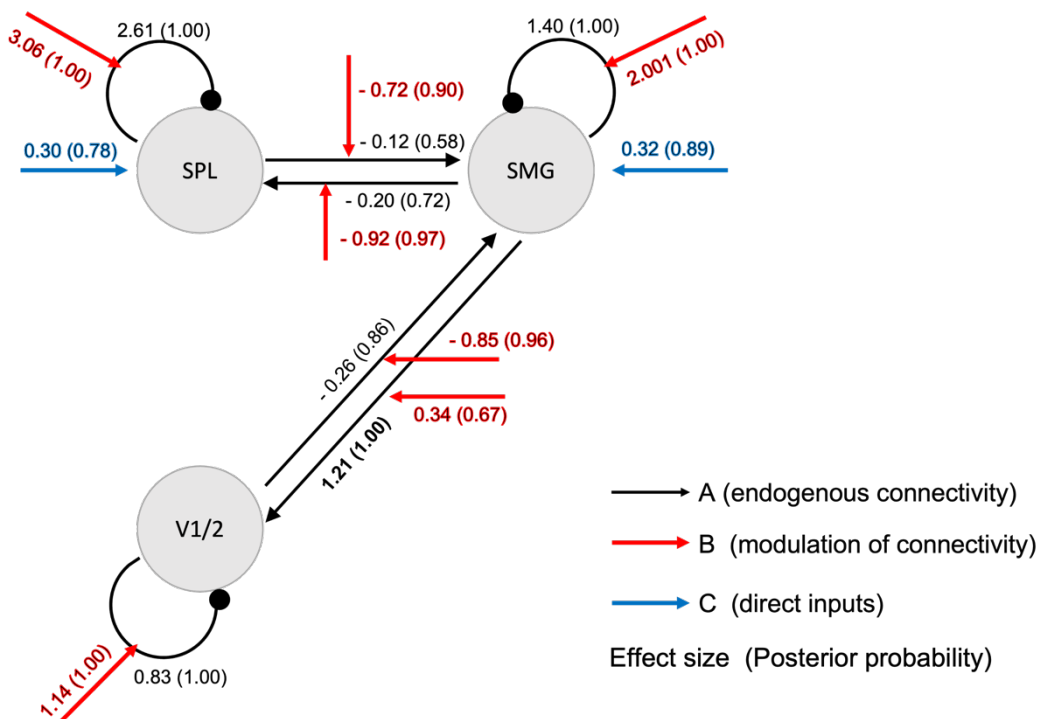


Figure 4: Results of BMR and BMA after the PEB estimation for the physical inference task. Network of estimated effect parameters and posterior probabilities into parentheses of the fixed connectivity (A matrix, black), modulatory inputs (B matrix, red), and driving inputs (C matrix, blue) during the physical inference task.

The results of the PEB estimation of the physical inference task showed significant driving inputs on SPL ($pe = 0.30\text{Hz}$, posterior probability = 0.78) and SMG ($pe = 0.32\text{Hz}$, posterior probability = 0.89), increased self-inhibition of all three areas ($pe = 3.06$ for SPL, 2.00 for SMG, 1.14 for V1/2, all with posterior probability = 1.00), increased top-down excitatory modulation from SMG to visual cortex ($pe = 0.34\text{Hz}$, posterior probability = 0.67), and increased bottom-up inhibitory modulation from visual cortex to SMG ($pe = 0.85\text{Hz}$, posterior probability = 0.96). The results also showed significant increased bi-directional inhibitory modulation between SPL and SMG ($pe = 0.72\text{Hz}$, posterior probability = 0.90 for SPL to SMG, and $pe = 0.92\text{Hz}$, posterior probability = 0.97 for SMG to SPL).

3.2. Influence of perception on connectivity

The same procedure was applied to the perception task, and the results of the PEB estimation showed significant driving inputs on SPL (effect size = 0.30Hz, posterior probability = 0.84), increased self-inhibition of SPL (pe = 1.00, posterior probability = 0.99) and SMG (pe = 0.56, posterior probability = 0.86), and decreased self-inhibition of early visual cortex (pe = 2.04, posterior probability = 1.00) (figure 5). Regarding modulatory inputs, results showed increased top-down excitatory modulation from SPL to visual cortex (pe = 0.47Hz, posterior probability = 0.79), and decreased excitatory modulation from SPL to SMG (pe = 1.11Hz, posterior probability = 1.00).

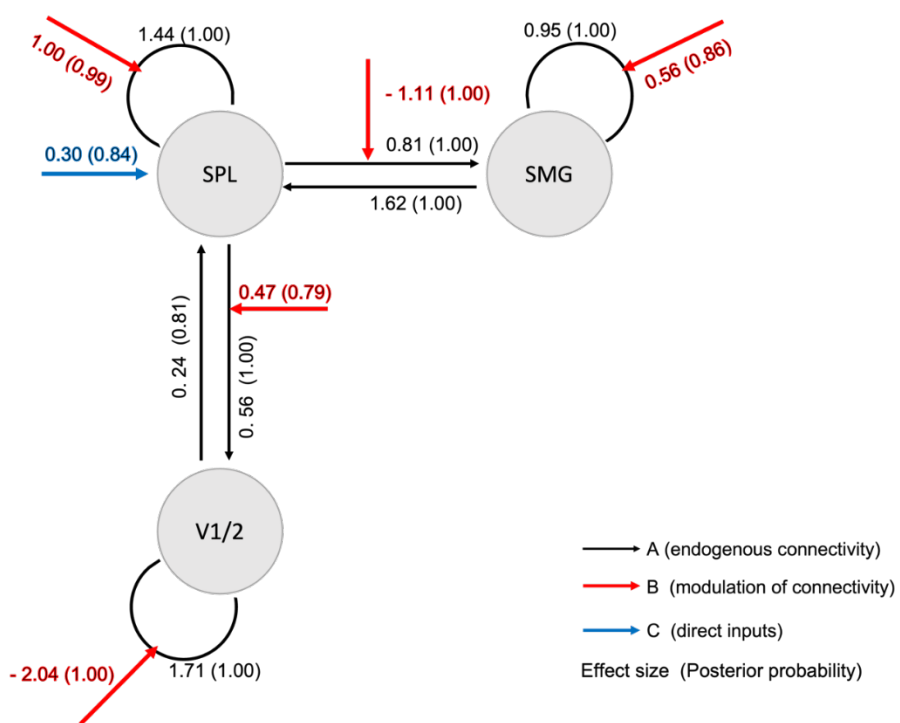


Figure 5: Results of BMR and BMA after the PEB estimation for the perception task. Network of estimated effect parameters and posterior probabilities into parentheses of the fixed connectivity (A matrix, black), modulatory inputs (B matrix, red), and driving inputs (C matrix, blue) during perception task.

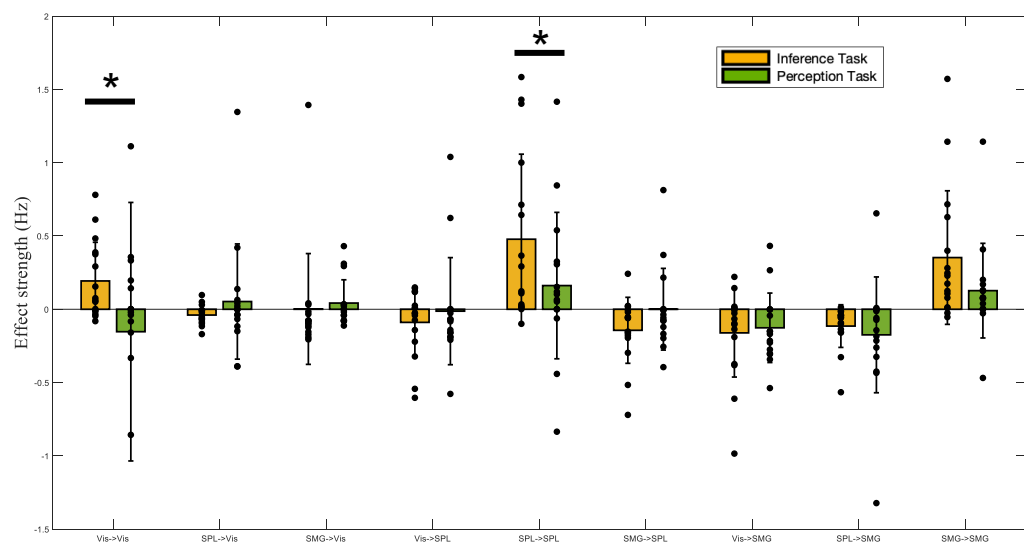
3.3. Comparison of connectivity strength during physical inference and perception

The classical paired t-test comparisons of the estimated single-subject modulation parameters from the full PEB models did not reveal any significant differences between physical inference and perception on between-region connectivity ($t(15) \leq 1.3$, $p \geq 0.2$), but the physical inference task showed greater self-inhibition in visual cortex ($t(15) = 2.9$, $p < .05$) and SPL ($t(15) = 2.6$, $p < .05$) than the perception task (figure 6A).

We ran a second statistical analysis, for which we set a threshold of posterior probabilities at 0.7 and removed the single-subject estimations whose probabilities fell below this threshold from the

group comparison. This resulted in samples containing between 0 and 16 parameter estimates for the physical inference task, and all samples containing 16 parameter estimates for the perception task.

A



B

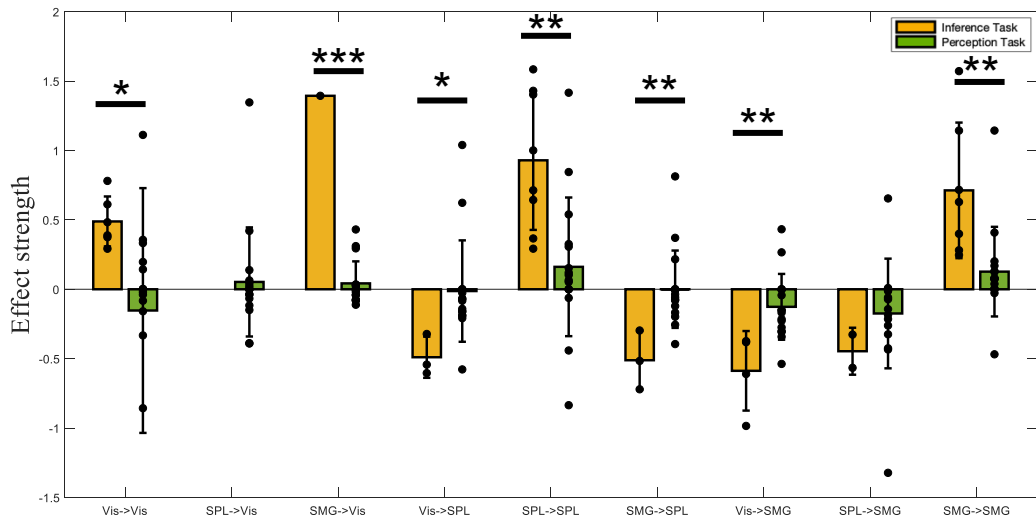


Figure 6: (A) Results of the paired t-tests between the physical inference and perception tasks based on all the subjects' estimated modulatory inputs of the full PEB model. Bonferroni-corrected comparisons that exhibit a statistically significant difference are indicated by asterisks, with * = $p < .05$. (B) Results of the second statistical analysis based on the subjects' estimated parameters that have posterior probabilities over 0.7. Bonferroni-corrected comparisons that exhibit a statistically significant difference are indicated by asterisks, with * = $p < .05$, ** = $p < .01$, *** = $p < .001$. The error bars in the two figures represent the standard deviations of each estimated parameter.

The results of the second analysis revealed significantly greater self-inhibition of all three brain regions in the physical inference task than in the perception task (visual cortex ($t(20) = 1.8$, $p <$

.05), SPL ($t(22) = 3.5$, $p < .01$) and SMG ($t(21) = 3.5$, $p < .01$) (figure 6B). The results also showed that the physical inference task has a significantly greater top-down excitatory modulation from SMG to visual cortex compared to the perception task ($t(15) = 10.0$, $p < .001$) and significantly greater bottom-up inhibitory modulations from visual cortex to SMG ($t(18) = 3.6$, $p < .01$) and to SPL ($t(17) = 2.2$, $p < .05$), as well as a significantly greater inhibitory modulation from SMG to SPL ($t(17) = 3.0$, $p < .01$).

4. Discussion

Our main goal was to use DCM and PEB to estimate and compare driving and modulatory inputs between physical inference and perception of falling objects, in a network of brain regions that are engaged in both tasks.

Our hypotheses are based on previous studies which revealed that both physical inference and perception involve overlapping brain areas (i.e., in parietal and visual cortex). It has been suggested that during physical inference, visual activity reflects visual imagery (12), whereas perception involves the processing of external visual inputs. Therefore, our first hypothesis was that during physical inference, driving inputs would enter the network via higher-order cognitive brain areas (i.e., the SPL and/or SMG) and modulatory inputs would predominantly strengthen top-down connections to visual regions. Our second hypothesis was that during the perception task, the presence of external visual inputs would be reflected in our DCM as driving inputs to the early visual regions, along with predominant modulations of bottom-up connections.

The results of our DCM analysis of the physical inference task largely support our first hypothesis. The PEB estimation results showed significant increased connectivity from SMG to visual (i.e., top-down connection) and decreased connectivity from visual to SMG (i.e., bottom-up connection), together with significant driving inputs to SMG and SPL during physical inference. Thus, we can speculate that the increased top-down connectivity reflects a transmission of physics-related information to the visual areas, which underlies the formation of visual representations of the trajectory. This may allow subjects to virtually “see” the trajectory of the falling ball in their mind’s eye.

In contrast, during the perception task, the results of our DCM analysis showed that visual cortex activity was explained by decreased self-inhibition rather than by direct driving input, and by increased top-down connectivity from the SPL, which goes against our second hypothesis. We also did not find significant increases in bottom-up connectivity from visual to parietal regions during perception, which is not in line with previous literature (7). One potential explanation for the unexpected results observed in the perception task could be related to the limited number of volumes acquired (i.e., 180). A low number of volumes could have reduced the signal-to-noise ratio, which can lead to spurious effects while limiting the statistical power of the analysis. Another potential explanation for the unexpected results could be related to the nature of the perception task itself, or the fact that it was followed by an inference task featuring a similar scenario.

To formally compare the DCM results of the physical inference and perception tasks, we compared the parameters estimates between the two tasks with frequentist statistics using Student’s t-test. The results showed that the only significant differences were greater self-inhibition in all three regions during physical inference compared to perception. However, this approach ignores the uncertainty at the between-subject level and assumes that every subject contributes equally well to the group estimation of parameters. Thus, we ran a second frequentist statistical analysis, in which we removed the single-subject estimates whose probabilities fell below a set threshold. This second analysis revealed significantly increased top-down connectivity from the SMG to visual areas, and significantly decreased bottom-up connectivity from visual to both

parietal areas during physical inference. However, this statistical analysis is limited by uneven sample sizes between the compared groups, together with small sample sizes and the somewhat arbitrary choice of the confidence threshold used to exclude datapoints, and should therefore be interpreted with caution. Overall, the results of comparison analyses served as additional components to complement the conclusions of PEB estimation approach. Nevertheless, in future analyses, we could apply more advanced DCM methods to help establish more robust conclusions. Also, in this study, the fMRI experiment used to investigate the neural mechanisms of physical inference in humans focused on a single body motion inference task and comparing it to a parallel perception task. However, in the future, other forms of object motion inference tasks should be designed to further develop our understanding of the neural dynamic networks involved in physical inference.

References

1. Battaglia, Peter W., Jessica B. Hamrick, and Joshua B. Tenenbaum. "Simulation as an engine of physical scene understanding." *Proceedings of the National Academy of Sciences* 110.45 (2013): 18327-18332.
2. Fischer, Jason, et al. "Functional neuroanatomy of intuitive physical inference." *Proceedings of the national academy of sciences* 113.34 (2016): E5072-E5081.
3. Winlove, Crawford IP, et al. "The neural correlates of visual imagery: A co-ordinate-based meta-analysis." *Cortex* 105 (2018): 4-25.
4. Albers, Anke Marit, et al. "Shared representations for working memory and mental imagery in early visual cortex." *Current Biology* 23.15 (2013): 1427-1431.
5. Friston, Karl J., Lee Harrison, and Will Penny. "Dynamic causal modelling." *Neuroimage* 19.4 (2003): 1273-1302.
6. Stephan, Klaas Enno, et al. "Ten simple rules for dynamic causal modeling." *Neuroimage* 49.4 (2010): 3099-3109.
7. Dijkstra, Nadine, et al. "Distinct top-down and bottom-up brain connectivity during visual perception and imagery." *Scientific reports* 7.1 (2017): 1-9.
8. Stephan, Klaas E., et al. "Translational perspectives for computational neuroimaging." *Neuron* 87.4 (2015): 716-732.
9. Zeidman, Peter, et al. "A guide to group effective connectivity analysis, part 1: First level analysis with DCM for fMRI." *Neuroimage* 200 (2019): 174-190.
10. Morris, Carl N. "Parametric empirical Bayes inference: theory and applications." *Journal of the American statistical Association* 78.381 (1983): 47-55.
11. Zeidman, Peter, et al. "A guide to group effective connectivity analysis, part 2: Second level analysis with PEB." *Neuroimage* 200 (2019): 12-25.
12. Ahuja, Aarit, Theresa M. Desrochers, and David L. Sheinberg. "A role for visual areas in physics simulations." *Cognitive Neuropsychology* 38.7-8 (2021): 425-439.
13. Eickhoff, Simon B., et al. "A new SPM toolbox for combining probabilistic cytoarchitectonic maps and functional imaging data." *Neuroimage* 25.4 (2005): 1325-1335.

A. Appendix

Cluster	JuBrain V3.0 Atlas	Harvard-Oxford Atlas	Size (voxels)	T	Peak location		
1	Occipital lobe L Area hOc1 [V1] 19.9%	Supracalcarine Cortex 5.9%	362	7.39	-30	-64	-2
2	Frontal lobe R Area 6mr / preSMA 1.3%	Paracingulate Gyrus 70.0% Superior Frontal Gyrus 5.0%	350	6.71	2	18	46
3	Parietal lobe R (SMG) Area hIP1 (IPS) 45.1% Area hIP2 (IPS) 38.1% Area PGa (IPL) 5.7% Area hIP3 (IPS) 4.9%	Angular Gyrus 32.0% Supramarginal Gyrus, posterior division 26.0%	296	5.39	44	-46	48
4	Parietal lobe R Area 7A (SPL) 27.8% Area 7P (SPL) 22.3%	Lateral Occipital Cortex, superior division 39.0% Precuneous Cortex 12.0%	256	6.31	12	-66	56
5	Parietal lobe L Area 7A (SPL) 26.4% Area hIP8 (IPS) 21.9% Area 7P (SPL) 20.8%	Lateral Occipital Cortex, superior division 50.0% Precuneous Cortex 12.0%	248	6.23	-12	-72	54
6	Frontal lobe R Area 6d3 9.5%	Middle Frontal Gyrus 31.0% Precentral Gyrus 13.0%	243	6.39	32	0	54
7	Occipital lobe L Area hOc4d [V3A] 49.8% Area hOc3d [V3d] 44.2% Area hOc2 [V2] 6.0%	Occipital Pole 44.0% Lateral Occipital Cortex, superior division 17.0%	210	6.72	-20	-92	22
8	R	Frontal Pole 67.0% Middle Frontal Gyrus 3.0%	87	5.89	38	42	24
9	Occipital lobe R Area hOc1 [V1] 20.7%		79	5.53	22	-78	2
10	Occipital lobe R Area hOc3v [V3v] 38.5% Area hOc2 [V2] 5.0%	Cerebellum Right VI 90.5% Cerebellum Right Crus I 4.8%	62	5.37	22	-70	-20

Table 1: This table summarizes the clusters that are identified by the GLM group-level t-test (Simulation > Control) analysis, which only includes the clusters larger than 50 voxels (13).

Cluster	JuBrain V3.0 Atlas	Harvard-Oxford Atlas	Size (voxels)	T	Peak location		
1	Occipital lobe L Area hOc5 [V5/MT] 9.1% Area hOc4la 8.8%	Lateral Occipital Cortex, inferior division 26.0% Middle Temporal Gyrus, temporooccipital part 22.0%	403	8.12	-52	-62	12
2	Area hOc5 [V5/MT] 26.1% Area hOc4la 11.2% R	Lateral Occipital Cortex, inferior division 33.0% Lateral Occipital Cortex, superior division 15.0%	389	9.89	42	-62	14
3	Parietal lobe R Area 7P (SPL) 66.0% Area 7A (SPL) 11.9%	Lateral Occipital Cortex, superior division 55.0% Precuneous Cortex 10.0%	120	6.18	14	-76	50
4	Area hIP3 (IPS) 36.5% R Area hIP1 (IPS) 33.6% Area hIP2 (IPS) 20.3%	Supramarginal Gyrus, posterior division 31.0% Superior Parietal Lobule 6.0%	77	5.1	38	-38	38
5	Area PF (IPL) 41.1% R Area PFt (IPL) 22.6%	Supramarginal Gyrus, anterior division 84.0% Postcentral Gyrus 2.0%	59	5.45	60	-28	46
6	Frontal lobe L Area 44 64.8%	Inferior Frontal Gyrus, pars opercularis 35.0% Precentral Gyrus 32.0%	57	5	-50	8	22
7	Area PFt (IPL) 65.9% L Area PF (IPL) 17.5% Area PFop (IPL) 1.1%	Supramarginal Gyrus, anterior division 50.0% Postcentral Gyrus 26.0%	45	5.64	-58	-28	40

Table 2: This table summarizes the clusters that are identified by the GLM group-level t-test (Positive effects of localizer Fall) analysis, which only includes the clusters larger than 30 voxels.